Supplementary Information

Wrinkled 2D Hybrid Heterostructures for Stretchable and Sensitive Photodetectors

*Hsu-Yen Lee[a, Δ], Guan-Zhang Lu[a, Δ], Ji-Lin Shen[b], Hsia-Yu Lin[a] and Yang-Fang Chen[a, *]*

[Δ] *Both the authors contributed equally*

[a] Department of Physics, National Taiwan University, Taipei 106, Taiwan

[b] Department of Physics, Chung Yuan Christian University, Taoyuan 320, Taiwan

[*] corresponding author: Yang-Fang Chen: yfchen@phys.ntu.edu.tw

Content

S8. Repeatability and stability of the hybrid wrinkled devices performance

S1. Device fabrication process

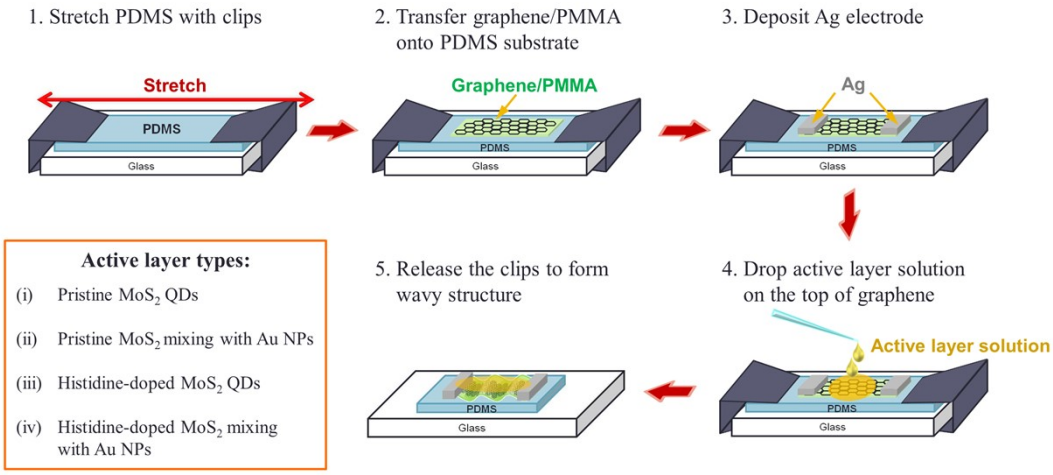

Fig. S1 Scheme of the device fabrication process.

S2. Characterization of histidine-doped MoS_2 quantum disks

The sizes and dimensions of the histidine-doped MoS_2 QDs were investigated by transmission electron microscopy (TEM) as shown in **Fig. S2a**. It is observed that the MoS_2 QDs possess a nanodisk structure.[1-3] An average size of 5.5 nm in diameter can be acquired from the histogram of a Gaussian fitting in the range from 3.5 to 6.5 nm. (inset of **Fig. S2a**) The thickness of single layer MoS_2 QD is 0.7 ~ 0.8 nm and the average layer number is around 6 layers. The high resolution TEM (HR-TEM) image of the MoS_2 QDs, as shown in **Fig. S2b**, indicates the (100) crystal plane of MoS_2 with a lattice spacing of around 0.27 nm and reveal a high crystalline structure with continuous lattice fringes.[2,4-8] Our previous publications[9,10] show more information of the characterization of the MoS_2 QDs.

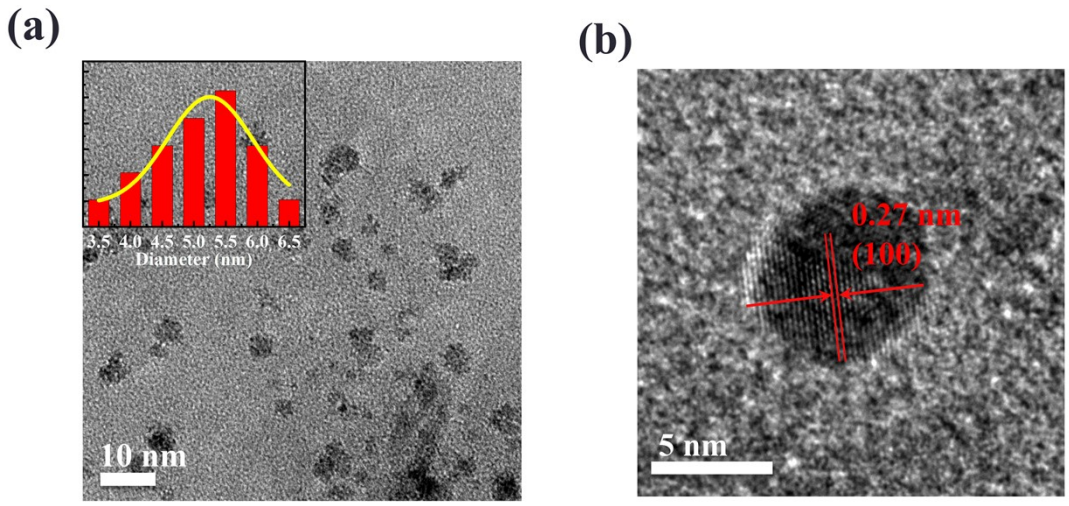

Fig. S2 (a) TEM image of histidine-doped MoS_2 QDs; inset of (a) shows the size distribution of the histidine-doped MoS_2 QDs. (b) High-resolution TEM image of MoS_2 QDs.

S3. Electrical properties of the wrinkled hybrid heterostructured photodetectors

The photocurrent and the dynamic photoresponse of the pristine MoS_2 QD/graphene without Au NP devices were studied as shown in **Fig. S3a(i)** and **b(i)**. After incorporating pristine MoS_2 QD with the planar graphene, the photocurrent is observed to increase significantly, which is much larger than that of the pristine MoS_2 QD alone. Compared with the planar device, the photocurrent of the wrinkled structure apparently increases more.

To further investigate the photoresponse of the pristine MoS_2 QD/graphene mixing with Au NP, the electrical measurements under the identical conditions were performed, as shown in **Fig. S3a(ii)** and **b(ii)**. The photocurrent of the wrinkled hybrid

device with Au NP is greater than the planar MoS_2 QD/graphene with Au NP and the pristine MoS_2 QD blending with Au NP.

In **Fig. S3c** and **d**, the responsivity R and specific detectivity D^* between the hybrid devices with and without Au NP are compared. It is clear that after depositing pristine MoS_2 QDs onto graphene, the R and D^* enhance drastically. Additionally, while considering the devices with Au NP, the enhancement of the R and D^* can also be clearly seen, indicating the effect of SPR. The calculation method of the responsivity and specific detectivity is shown in the **Supplementary Information S4**.

Subsequently, the photocurrent (I_{ph}-V curves) and the dynamic photoresponse (I-T curves) of different structures of the hybrid photodetectors based on histidine-doped MoS_2 QDs were displayed in **Fig. S4a** and **b**, respectively. Similar to the photodetectors based on pristine MoS_2 QD, the photocurrent of the histidine-doped MoS_2 QDs/graphene without Au NP on the wrinkled device increases the most compared with that of the planar MoS_2 QDs/graphene, and the photocurrent of the pure histidine-doped MoS_2 QDs device is the minimum one among these three types of the structure, as shown in **Fig. S4a(i)** and **b(i)**. After blending histidine-doped MoS_2 QD with Au NP and repeating the photodetection measurements, all of the photocurrent of the hybrid devices with Au NP exhibit the same trend as the devices without mixing with Au NP. The photocurrent of the wrinkled device with Au NP is enhanced more than that of the

planar MoS_2 QDs/graphene device with Au NP. These results are shown in **Fig. S4a(ii)** and **b(ii)**.

In **Fig. S4c**, the value of R of the histidine-doped MoS_2 QDs/graphene wrinkled photodetector with Au NP is ~ 2.1 and 1.5 times larger than the wrinkled hybrid device without Au NP and the planar hybrid device with Au NP, respectively. Besides, the D^* of the wrinkled hybrid photodetector with Au NP is ~ 2.0 times larger than the planar MoS_2 QDs/graphene device with Au NP in **Fig. S4d**.

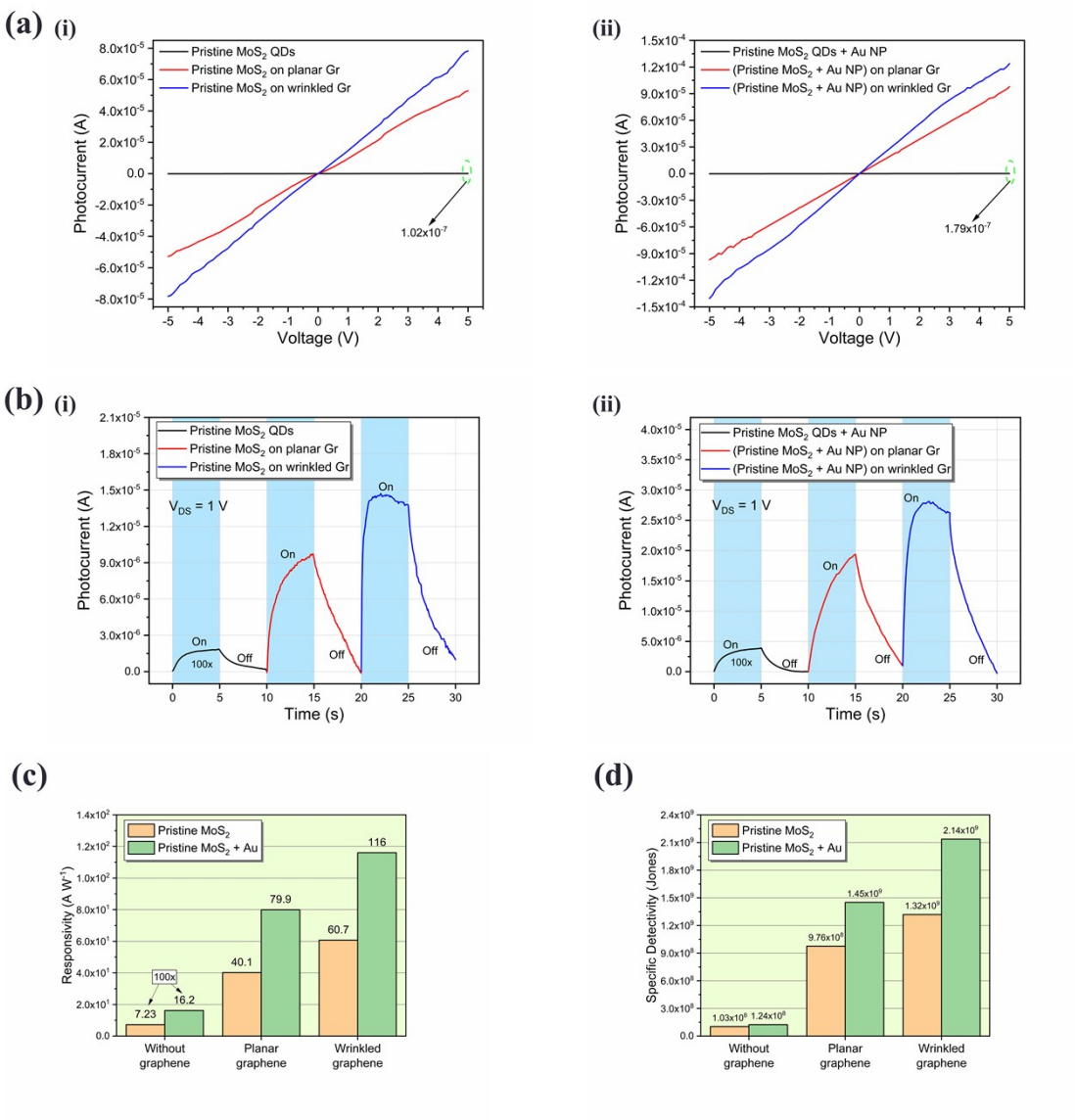

Fig. S3 (a) I_{ph}-V curves of three types of the pristine MoS_2 QD/graphene hybrid devices (i) without Au NPs and (ii) with Au NPs. (b) I-T curves of three types of the pristine MoS_2 QD/graphene hybrid devices (i) without Au NPs and (ii) with Au NPs. All the I-V curves are measured under 325 nm laser illumination of power density of 1.21 mW cm^{-2} and all the I-T curves are biased at 1 V. (c) Responsivity and (d) specific detectivity comparisons of the pristine MoS_2 QD/graphene hybrid devices with and without mixing Au NPs under 325 nm excitation of power density of 1.21 mW cm^{-2} and biased at 1 V.

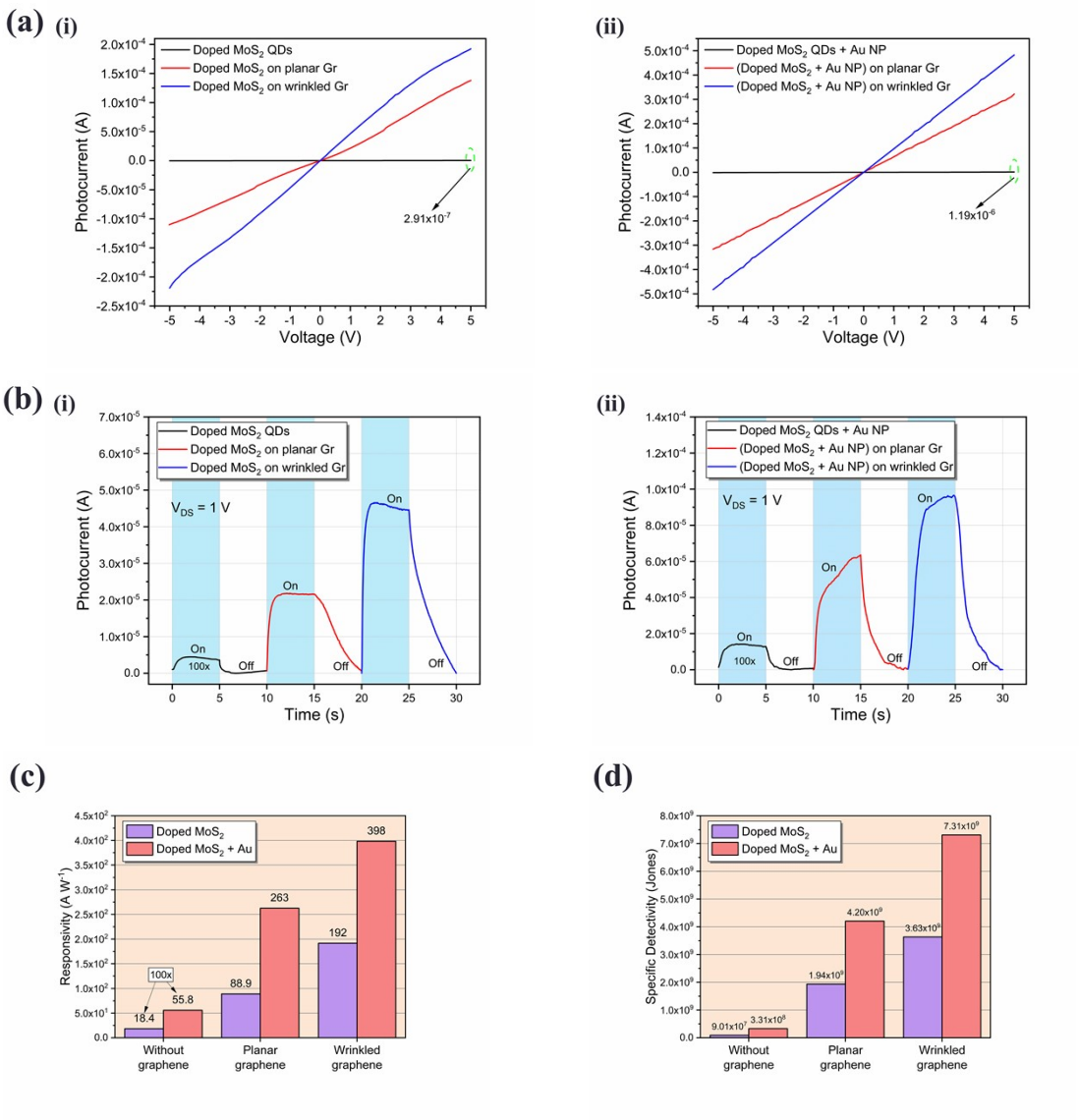

Fig. S4 (a) I_{ph}-V curves of three types of the histidine-doped MoS_2 QD/graphene hybrid devices (i) without Au NPs and (ii) with Au NPs. (b) I-T curves of three types of the histidine-doped MoS_2 QD/graphene hybrid devices (i) without Au NPs and (ii) with Au NPs. All the I-V curves are measured under 325 nm laser illumination of power density of 1.21 mW cm^{-2} and all the I-T curves are biased at 1 V. (c) Responsivity and (d) specific detectivity comparisons of the histidine-doped MoS_2 QD/graphene hybrid

devices with and without Au NPs under 325 nm excitation of power density of 1.21 mW cm^{-2} and biased at 1 V.

S4. Photodetection performance calculation

In the identical experimental conditions, the performance of specific photoelectric devices can be investigated through responsivity and specific detectivity.[11,12]

Responsivity:

Responsivity (R) is the ratio between the photocurrent and the total incident optical power on the photodetector in A/W, which is defined as

$$R = \frac{I_{ph}}{P_{in}} \quad \text{(i)}$$

where P_{in} is the power irradiated on the active region of the photodetector in W and I_{ph} is the photocurrent in A and equal to $|I_{light} - I_{dark}|$. I_{light} is the current with illumination and I_{dark} is the current without illumination. It represents the conversion of the optical-to-electrical signal.[12]

Specific detectivity:

For the device containing graphene as a conduction channel, the graphene layer has a high charge carrier mobility and good conductivity, the dark current is dominated by the shot noise as shown in many published reports. One of the better ways to enlarge the detectivity is to open the energy gap of graphene to reduce the dark current.

Therefore, we chose the dark current to evaluate the specific detectivity under the assumption of a shot-noise limited device.[12-14] Specific detectivity (D^*) represents the sensitivity of the photodectector to capture weak signal from noise and is defined as

$$D^* = \frac{R\sqrt{A}}{\sqrt{2eI_{dark}}} \quad \text{(ii)}$$

where A is the effective area of the photodetector, e is the elementary electron charge, and I_{dark} is the current without illumination.[11]

S5. Transient photoresponse measurement of the MoS_2 QD/graphene hybrid devices

The temporal photoresponse of the MoS_2 QD/graphene hybrid wrinkled devices were measured, as shown in **Fig. S5**. Based on the mechanism of the doping technologies and fundamental physics of semiconductors, as the doping concentration increases, the Fermi level will keep away from the intrinsic Fermi level which is around at the middle of the energy band gap. The intrinsic Fermi level is the Fermi level of undoped semiconductors, such as Si, WSe_2, $ReSe_2$, and MoS_2. According to the energy band diagram as shown in **Fig. 4d**, as the doping concentration of histidine increases, the depletion width and the built-in electric field will increase. On the other hand, according to some published manuscripts[15, 16], the more expanded depletion width, the stronger built-in electric field in the interface between each other semiconductors,

making it easier to collect the photogenerated carriers, and the photoresponse (rising time) becomes faster than the undoped (pristine) devices. Additionally, doping of MoS_2 QDs by histidine may be able to passivate defects, which enables to increase the photo-gain and reduce the response time.

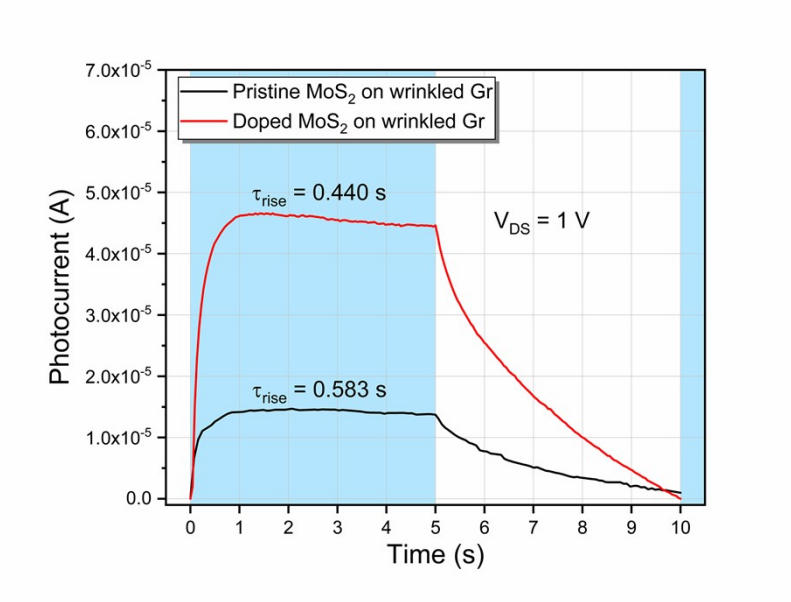

Fig. S5 Dynamic response time comparison of the pristine MoS_2 QD/graphene and the histidine-doped MoS_2 QD/graphene hybrid photodetector biased at 1 V under 325 nm laser illumination of power density of 1.21 mW cm^{-2}.

S6. Quantitative analysis between the strain and the height of the graphene wrinkles

To compute a quantitative relationship between the strain and the height of the graphene ripples, the strain ratio of different stretched state in wrinkled devices is depicted in **Fig. S6**. The strain S is given by

$$S = \frac{t - t_0}{t_0} \tag{iii}$$

where $2t_0$ and $2t$ is the crest width under 0% and arbitrary x% strain. Also, l is the length from the hill to the valley and h is the height of the wrinkle under arbitrary x% strain. At a n% prestretched device,

$$t_0 \times (100 + n)\% = l \tag{iv}$$

The relation between l and h is

$$l^2 = h^2 + t^2 \tag{v}$$

and it contributes to a quadratic approximation of strain varying with the height of the graphene wrinkle in **Eq. (v)**. Therefore, in the following discussions, the wrinkled structure accounts for 0% strain or the released state while fully released and the planar one is designated as 100% strain or the fully strained state while fully stretched.

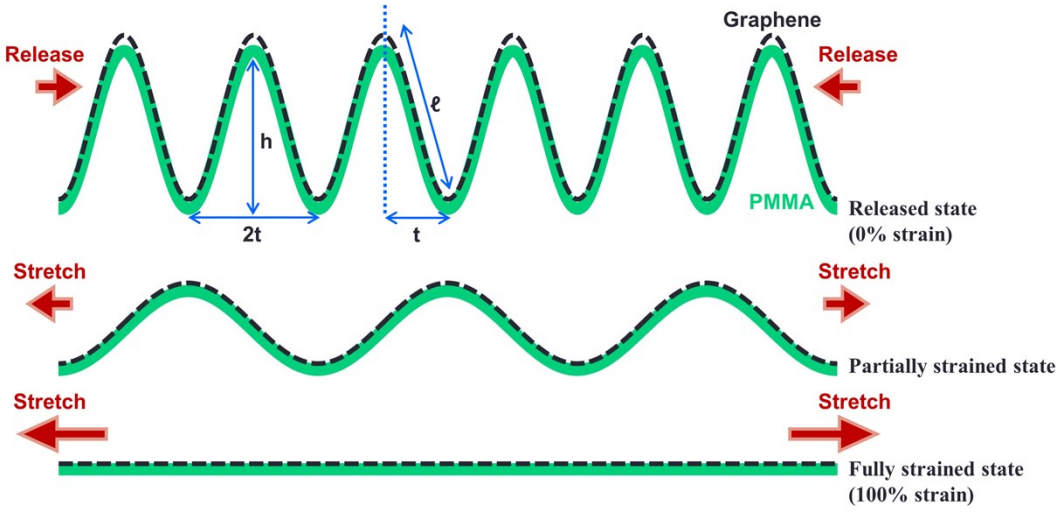

Fig. S6 Strain representation of the wrinkled graphene/PMMA structure.

S7. Optical absorption spectra of the various structures of the MoS_2 QD/graphene hybrid wrinkled photodetectors.

The absorption spectrum of the histidine-doped MoS_2 QD/graphene wrinkled device mixing with Au NPs is larger than the other two structures. It can be concluded that the scattering effect from Au NPs and the photo-confinement effect from the wrinkled structure facilitate the total absorption.

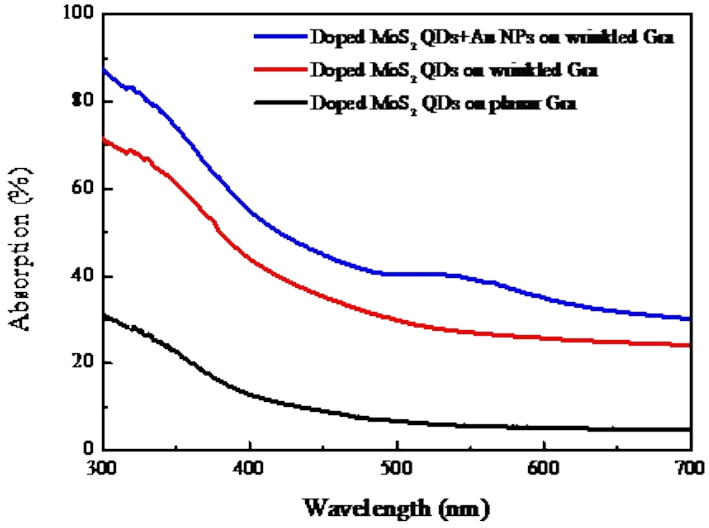

Fig. S7 Absorption spectra of the three types of the hybrid photodetectors.

S8. Repeatability and stability of the hybrid wrinkled devices performance

To understand the repeatability and stability of the device, the fatigue test of the histidine-doped MoS_2 QD/graphene hybrid wrinkled photodetectors was conducted by repeatedly stretching and releasing. One stretching and releasing cycle is defined as the device with the initial strain 0%, then stretching the device with the strain 100%. Next,

the strain of the device returns to 0% after releasing. The photocurrent of the device after applying strain at multiple times were recorded under 325 nm laser illumination, as shown in **Fig. S8**. It is clear that the hybrid wrinkled devices show an excellent repeatability and stability after stretched test, which is a very useful for practical application.

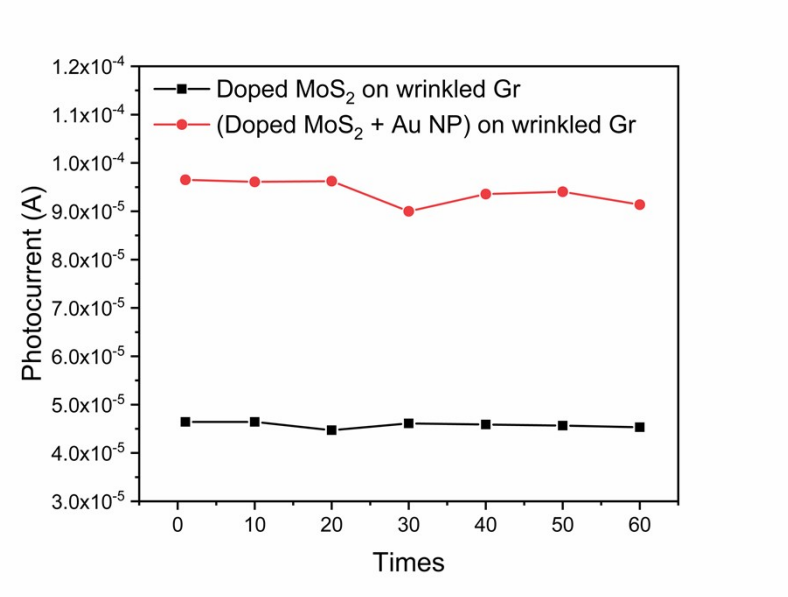

Fig. S8 Fatigue test of the histidine-doped MoS_2 QD/graphene hybrid wrinkled photodetectors with and without Au NPs after each cycle of stretching and releasing under 325 nm laser illumination of power density of 1.21 mW cm^{-2}.

References

1 W. Yin, X. Bai, X. Zhang, J. Zhang, X. Gao and W. W. Yu, *Part. Part. Syst. Charact.*, 2019, **36**, 1800362.

2 H. Lin, C. Wang, J. Wu, Z. Xu, Y. Huang and C. Zhang, *New J. Chem.*, 2015, **39**,

8492-8497.

3 D. Haldar, D. Dinda and S. K. Saha, *J. Mater. Chem. C*, 2016, **4**, 6321-6326.

4 R. P. Ojha, R. Mishra, P. Singh, N. R. Nirala and R. Prakash, *Mikrochim Acta*, 2019, **187**, 74.

5. Q. Liu, C. Hu and X. Wang, *RSC Adv.*, 2016, **6**, 25605-25610.

6 W. Qiao, S. Yan, X. Song, X. Zhang, Y. Sun, X. Chen, W. Zhong and Y. Du, *RSC Adv.*, 2015, **5**, 97696-97701.

7 Z. X. Gan, L. Z. Liu, H. Y. Wu, Y. L. Hao, Y. Shan, X. L. Wu and P. K. Chu, *Appl. Phys. Lett.*, 2015, **106**, 233113.

8 W. Dai, H. Dong, B. Fugetsu, Y. Cao, H. Lu, X. Ma and X. Zhang, *Small*, 2015, **11**, 4158-4164.

9 G. Z. Lu, M. J. Wu, T. N. Lin, C. Y. Chang, W. L. Lin, Y. T. Chen, C. F. Hou, H. J. Cheng, T. Y. Lin, J. L. Shen and Y. F. Chen, *Small*, 2019, **15**, e1901908.

10 Y. C. Chien, T. L. Shen, W. K. Wu, C. Y. Li, H. T. Chin, C. W. Chang, T. Y. Lin, S. H. Chang, J. L. Shen and Y. F. Chen, *Mater. Today Nano*, 2022, **18**, 100173.

11 J. Wang, J. Han, X. Chen and X. Wang, *InfoMat*, 2019, **1**, 33-53.

12. M. Buscema, J. O. Island, D. J. Groenendijk, S. I. Blanter, G. A. Steele, H. S. van der Zant and A. Castellanos-Gomez, *Chem. Soc. Rev.*, 2015, **44**, 3691-3718.

13. Y. Fang, A. Armin, P. Meredith and J. Huang, *Nat. Photonics*, 2019, **13**, 1-4.

14. G. Konstantatos, M. Badioli, L. Gaudreau, J. Osmond, M. Bernechea, F. P. Garcia de Arquer, F. Gatti and F. H. Koppens, *Nat. Nanotechnol.*, 2012, **7**, 363-368.

15. S. H. Jo, D. H. Kang, J. Shim, J. Jeon, M. H. Jeon, G. Yoo, J. Kim, J. Lee, G. Y. Yeom and S. Lee, *Adv. Mater.*, 2016, **28**, 4824-4831.

16. J. Kim, K. Heo, D. H. Kang, C. Shin, S. Lee, H. Y. Yu and J. H. Park, *Adv. Sci.*, 2019, **6**, 1901255.